Correspondence to:
S. M. Smith,
smsm@bu.edu

Characterization of a Double Mesospheric Bore Over Europe

Steven M. Smith[1] iD, Gunter Stober[2] iD, Christoph Jacobi[3] iD, Jorge L. Chau[2] iD, Michael Gerding[2] iD, Martin G. Mlynczak[4] iD, James M. Russell[5] iD, Jeffrey L. Baumgardner[1], Michael Mendillo[1], Monica Lazzarin[6] iD, and Gabriel Umbriaco[6] iD

[1]Center for Space Physics, Boston University, Boston, MA, USA, [2]Leibniz Institute for Atmospheric Physics, University of Rostock, Rostock, Germany, [3]Institute for Meteorology, University of Leipzig, Leipzig, Germany, [4]NASA Langley Research Center, Hampton, VA, USA, [5]Center for Atmospheric Sciences, Hampton University, Hampton, VA, USA, [6]Department of Physics and Astronomy, University of Padua, Padua, Italy

Abstract Observations of a pair of mesospheric bore disturbances that propagated through the nighttime mesosphere over Europe are presented. The observations were made at the Padua Observatory, Asiago (45.9°N, 11.5°E), by the Boston University all-sky imager on 11 March 2013. The bores appeared over the northwest horizon, approximately 30 min apart, and propagated toward the southeast. Using additional satellite and radar data, we present evidence indicating the bores originated in the mesosphere from a single, larger-scale mesospheric disturbance propagating through the mesopause region. Furthermore, the large-scale mesospheric disturbance appeared to be associated with an intense weather disturbance that moved southeastward over the United Kingdom and western Europe during 10 and 11 March.
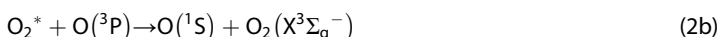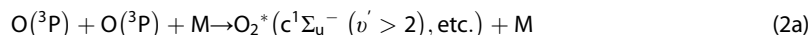
Plain Language Summary A large wave disturbance occurred in the upper atmosphere over western Europe in March 2013 and appeared to be associated with a large storm system that brought cold weather and snow to the UK and western Europe. The disturbance, called a bore, occurred in the Earth's mesosphere an altitude of 90--100~km. Little is known about the origin of mesospheric bores, but it would appear that surface weather activity may be a contributor to their formation in some cases.

1. Introduction

Mesospheric nightglow emission arises from naturally occurring chemoluminescence reactions. The brightest emissions arise from hydroxyl (OH) and atomic oxygen which originate from 87 km and 97 km, respectively. The majority of mesospheric OH emission is produced by the reaction of hydrogen and ozone (Bates & Nicolet, 1950):

$$H + O_3 \rightarrow OH(v \leq 9) + O_2 \tag{1a}$$

$$OH(v) \rightarrow OH(v - \Delta v) + hv \ (\text{Meinel band emission}) \tag{1b}$$
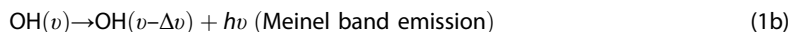
The emission consists of a series of emission bands, the Meinel bands, which occur throughout the visible and infrared spectral regions. The 557.7 nm emission due to O(^{1}S) arises via a collisional three-body reaction involving atomic oxygen and a neutral species (denoted as M and usually N_2 or O_2) known as the Barth reaction (Barth & Hildebrandt, 1961):

$$O(^3P) + O(^3P) + M \rightarrow O_2{}^* \left(c^1\Sigma_u{}^- \ (v' > 2), \text{etc.} \right) + M \tag{2a}$$

$$O_2{}^* + O(^3P) \rightarrow O(^1S) + O_2 \left(X^3\Sigma_g{}^- \right) \tag{2b}$$

$$O(^1S) \rightarrow O(^1D) + hv(557.7 \text{ nm}) \tag{2c}$$

Mesospheric bores are a type of gravity wave disturbance that occurs in the upper mesospheric nightglow and are characterized by a propagating step-like jump (a "bright" wave) or drop (a "dark" wave) followed by a resultant train of wavefronts (an undular bore) in the background emission (Dewan & Picard, 1998). Brightness enhancements and reductions of up to 30% have been recorded (Bageston et al., 2011, 2011b; Batista et al., 2002; Brown et al., 2004; Fechine et al., 2005, 2009; Medeiros et al., 2005, 2016;

Narayanan et al., 2009; Nielsen et al., 2006; She, Li, et al., 2004; Shiokawa et al., 2006; Smith, 2013; Smith et al., 2003, 2005; Taylor et al., 1995; Walterscheid et al., 2012; Yue et al., 2010). Mesospheric bores have been observed in most geographical regions, yet little is known about the processes responsible for their formation and evolution.

Mesospheric bores require a stable layer or duct, such as a temperature inversion or a wind shear, in which to propagate (Dewan & Picard, 1998, 2001). The depth of the propagation duct determines the propagation speed of a mesospheric bore [$U \propto (\text{duct depth})^{1/2}$] and also the degree of associated undularity or turbulence. For an initial duct depth of h_0, the bore will propagate with speed:

$$U_{\text{bore}} = \sqrt{g' \frac{h_1(h_1 + h_0)}{2h_0}}$$

(3)

Here h_1 is the disturbed depth due to the bore and g' is the acceleration due to gravity corrected for buoyancy. Functionally, $g' = g\,\Delta\varphi/\varphi$, where φ is the mean potential temperature at the bore altitude and $\Delta\varphi$ is the change in potential temperature between h_0 and h_1 (Dewan & Picard, 1998). Ducted wave propagation tends to experience less wave attenuation, allowing the transportation of wave energy and momentum to large horizontal distances (~1000 km) (e.g., Smith et al., 2003).

Bores dissipate the majority of their energy in the antipropagation direction and, as a result, may generate a train of trailing waves behind the leading front (an undular bore) or a trailing region of turbulence (a turbulent bore) (Lighthill, 1978). The degree of undularity or turbulence can be predicted using the normalized bore strength defined as $\beta = (h_1 - h_0)/h_0$ (Lighthill, 1978). In general, trailing turbulence occurs when $\beta > 0.3$, and undularity when $\beta < 0.3$. Dewan and Picard (1998) derived a relationship describing the hourly rate production of trailing waves (dW/dt) in a mesospheric bore with trailing wave of amplitude, a (in km), as follows:

$$\frac{dW}{dt} = 1.8 \times 10^3 \ \frac{U_{\text{bore}}(h_1 - h_0)^3}{2a^2 \lambda_h h_1}.$$

(4)

Mesospheric bores are of scientific importance for several reasons. They tend to be associated with bright wave events, sometimes visible to the naked eye and, as such, are associated with larger amounts of wave energy compared to the typical subvisual mesospheric gravity waves. Furthermore, because mesospheric bores utilize ducted modes of propagation, they are capable of transporting wave energy and momentum over larger distances with lower attenuation than typical mesospheric gravity waves. And, although they occur infrequently at any one location (~1 per week), they have been observed over the entire range of latitudes, but their origin is still unclear and may originate via more than one mechanism.

Reports of double mesospheric bores are exceedingly rare. Medeiros et al. (2016) reported on a night in which two bores, separated by 3 h, propagated over two sites in Brazil separated by a distance of 85 km. The twin bore event we report on in this paper is remarkable because although the bores remained separated in time and space, (a) the bore onsets occurred within 30 min of each other, (b) they persisted as simultaneous and distinct features visible within the field of view of a single all-sky imager site, and (c) they propagated in similar directions.

2. Instrumentation and Data

The Boston University all-sky imager at the Padua Observatory, Asiago (45.9°N, 11.5°E), has been operating since early 2010 (Baumgardner et al., 2013; Mendillo et al., 2012, 2013). The imager is equipped with an Andor back-illuminated bare CCD camera and a 16 mm fish-eye lens which record several nightglow emissions over the entire 180° of the night sky. The imager records OH broadband emission (695–1050 nm) and narrowband O(^{1}S) (557.7 nm) emission from 87 km and 97 km, respectively, and from thermospheric O^{1}D (630.0 nm) emission from ~250 km. The OH and O(^{1}S) emissions originate from layers 8–10 km thick and so they can be exploited as dynamical tracers. The imaging system operates autonomously via a PC on a nightly basis during moonless periods. During each night, images are obtained on a continuous repeating cycle every 1–2 min with each particular filter been visited every 8–10 min. The location of Asiago and the field of view of the imager are shown in Figure 1.
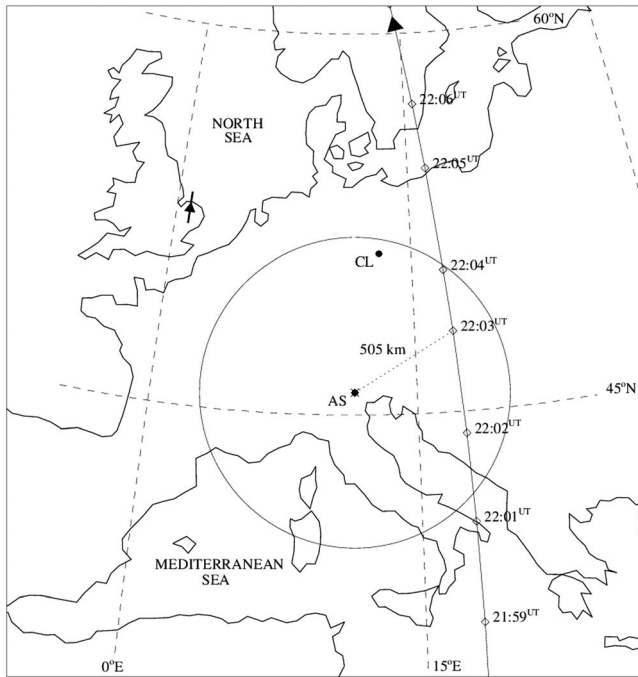
Figure 1. Map showing the locations of the Asiago site (AS), the Collm meteor radar (CL), and the ground track of the SABER measurements. The field of view of the all-sky imager to 5° elevation at 96 km altitude is shown as a solid circle. The location of the apparent center and origin of the curved wavefronts over SE England is also shown by the triangle $\pm\sigma$ (see text).

Reduction of the raw all-sky images involved utilizing standard procedures, initial bias and dark subtraction, followed by flat fielding to remove effects of vignetting due to the imaging system, van Rhijn brightening, and atmospheric extinction (see Baumgardner et al., 2007, for a fuller description). A routine was then used to remove stars and reduce the effect of the Milky Way. The routine scans though each image and finds the median of each 8×8 pixel region and calculates the deviation from the median relative to the 25th and 75th percentiles. Large deviations are probably due to stars and so those pixels are replaced by the median value. The images were also mapped onto the Earth's surface using known star positions within each image and the nominal heights of the emission layers (OH ~87 km, O(^{1}S) ~97 km), a process called unwarping.

Supporting observations came from two sources. Neutral temperature and OH emission profiles were obtained from the SABER instrument aboard the NASA TIMED (Thermosphere, Ionosphere, Mesosphere Energetics and Dynamics) satellite (http://saber.gats-inc.com) during an overpass above the Asiago site that occurred 4 h prior to the event. The SABER measurements were obtained within 505 km of Asiago, and the ground track is shown in Figure 1. Complementing the one-time satellite data were neutral wind profiles from the 70–100 km altitude region obtained by the Collm meteor radar facility in Germany (51.3°N, 13.0°E). The radar is located 610 km north of Asiago and is denoted as "CL" in Figure 1, inside the field of view of the imager.

3. Observations

3.1. All-Sky Imaging

Figure 2 shows a sequence of images in the O(^{1}S) emission during the 2 h period of 02:13–04:05 UT on 11 March 2013 (Figures 2a–2f). They portray the time evolution of the double bore disturbance in the O(^{1}S) nightglow propagating over the Asiago Observatory. For clarity, Figures 2g–2i show tracings delineating the major frontal features of the bores shown in Figures 2a–2c of the same figure. The image scale depicted in Figure 2 (unwarped images) is smaller than in Figure 1 in order to show the details associated with the bores. As a result, the location of the Collm radar is not shown in Figure 2 because it lies outside, to the north, of the border of the panels. Movies of the bores in the O(^{1}S) and OH emissions are available as the supporting information attached to this paper.

The initial disturbance was characterized by a large-scale, step-like enhancement in the background emission, a feature typical of a mesospheric bore. The first bore appeared near the northwestern horizon at 02:06:27 UT propagating toward the southeast at an azimuth of 138° ± 1°. Cloud cover precluded earlier observations. The leading disturbance consisted of a train of bright wavefronts with a mean horizontal wavelength $\lambda_h = 34.7 \pm 3.7$ km that propagated with a mean phase speed of $c_{obs} = 80.1 \pm 2.6$ ms^{-1}. The wavefronts were markedly curved and extended over almost 800 km across the sky. In particular, the double bores both exhibited morphology and behaviors consistent with the eight criteria devised for bore identification by Dewan and Picard (2001). The bore criteria used were as follows:

1. The first criterion is an extensive frontal boundary separating light and dark regions of airglow that propagates at 20–100 ms^{-1}.
2. The front will be accompanied by either a series of trailing waves (an undular bore) or a region of turbulence (a nonundular or turbulent bore).
3. A thermal inversion layer must be present at the altitude of the bore in order to act as a ducting region for the bore to propagate within. A wind shear may also provide such a region.
4. Images of different airglow layers will exhibit wave patterns that are either in phase or 180° out of phase with each other, depending on the relative altitudes of the layers.
5. The speed and wavelength of the bore will obey equations (12) and (13) of Dewan and Picard (1998).
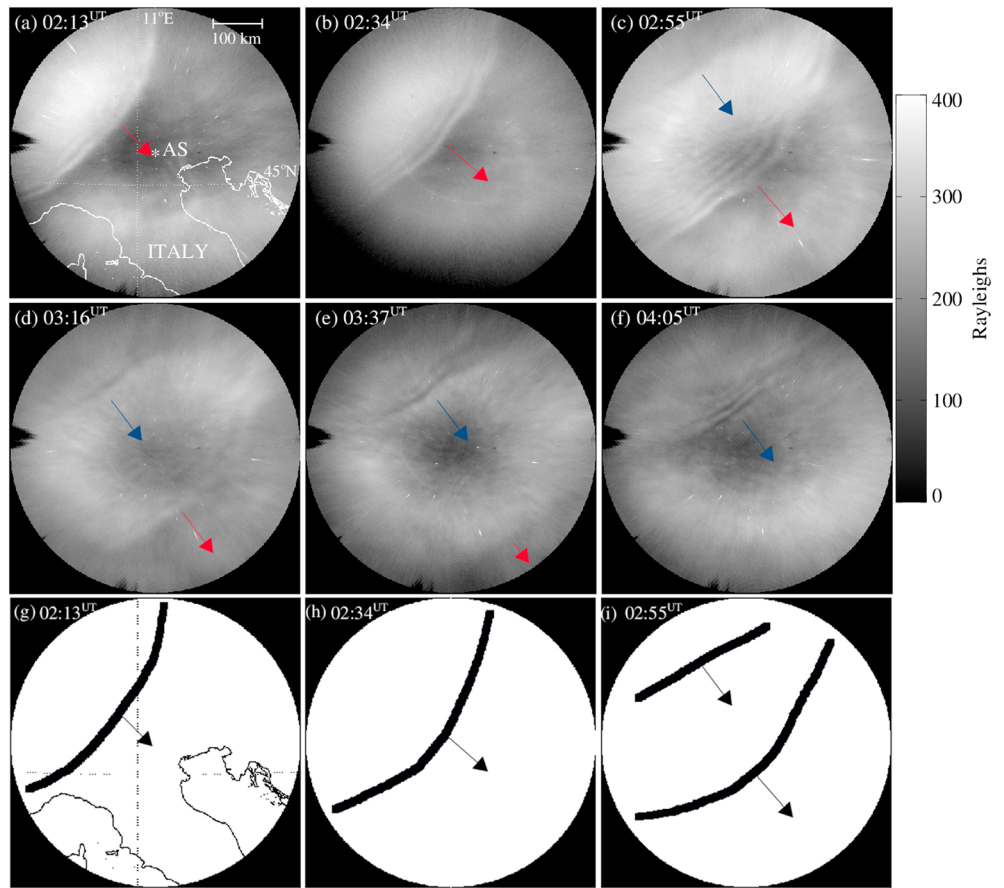
Figure 2. Sequence of unwarped O(^{1}S) (557.7 nm) all-sky images showing the southeastward propagation (arrowed) and time evolution of the dual bore disturbances over the Asiago observatory on 11 March 2013. (a–d) The first bore (red arrow) and (c–f) the second bore (blue arrow). (g–i) The major frontal features of the bores shown in Figures 2a–2c.

6. The number of trailing waves associated with undular bores increases with time (~2 or more waves per hour) as the bore dissipates energy into the duct; assuming no energy is lost from the duct.
7. The temperature change ΔT across the front should agree approximately with
8. $(h_1 - h_0) \times 10$ K/km$^{-1} = \Delta T$.
9. The occurrence of a bore event may be associated with strong gravity wave sources.

Figure 3 shows the O(^{1}S) (557.7 nm) zenith brightness over Asiago during the course of the night. The mean brightness over a 9 × 9 pixel area at zenith (~3 x 3 km at 96 km) was used. During the passage of the bore, the zenith O(^{1}S) airglow brightness increased from 210 R to 370 R (75%) over a period of 45 min. The zenith crossing time of the first bore is marked in Figure 3 as the vertical dashed line.

Typical airglow brightness enhancements associated with frontal gravity waves in the mesosphere and lower thermosphere (MLT) are 5–20% so the 75% enhancement associated with the Asiago bore event represents one of the largest enhancements ever recorded. The largest recorded enhancement of 109% being associated with the Texas bore event (Smith et al., 2003). In contrast, the response in the OH emission at ~87 km was very weak (not shown) which indicates that the altitude of the disturbance, and hence the ducting region, was significantly higher than the centroid altitude of the OH emission.

A second bore appeared above the northwestern horizon at 02:34 UT (28 min after the first event) and also propagated southeastward. In the O(^{1}S) emission, the bore propagated with a mean phase speed of $c_{obs} = 53.7 \pm 8.4$ ms^{-1} and a propagation azimuth of 147° ± 1° (a difference of 9° in relation to the first bore event). The O(^{1}S) airglow also exhibited a dark response, that is, the bore caused a 10–15% decrease in the background airglow brightness during the first half hour of its appearance. Image cross sections through
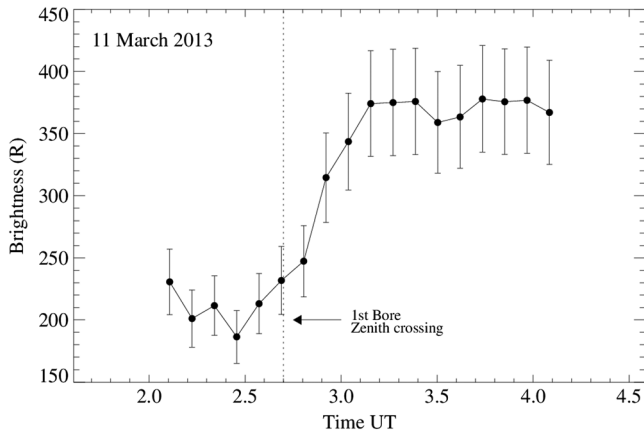
Figure 3. Plot of the O(^{1}S) 557.7 nm zenith brightness during night's 2 h observation period. The zenith passage of the first bore (dashed vertical line) was associated with a 75% enhancement in airglow emission.

each image along the direction of the bore propagation were analyzed to determine the airglow response to the bore disturbance.

The wavefronts were linear in shape (unlike in the first bore, which were curved), and the leading wavefront spanned a shorter horizontal extent across the sky than the first event (by ~2 times) (see Figures 2d–2f). In addition, the mean wavelength of the first bore in the O(^{1}S) airglow was $\lambda_h = 34.4 \pm 6.3$ km. Initially, the bore appeared to be turbulent, but after ~0.5 h, the first trailing wave appeared (Figure 2d), which suggests that the duct depth decreased during that time period. The observation period ended before the second bore passed over the Asiago site.

In the OH emission (images are available in the supporting information), the second bore was brighter than the first and exhibited an emission enhancement similar to the bore in the O(^{1}S) emission, both of 10–12%. The mean horizontal wavelength of the trailing OH waves was similar to that exhibited by the first OH bore (see Table 1). Table 1 lists the measured parameters associated with both bore events.

In both bore events, at any time, the horizontal wavelength of the trailing waves in the train (the individual wavefronts) decreased away from the leading front, suggesting dispersion effects or nonlinear, soliton-like behavior of the individual wavefronts. However, during the course of the bore events, the horizontal wavelengths of the first O(^{1}S) bore decreased, which indicated that the mutual proximity of individual wavefronts decreased as time progressed. This behavior is unusual for a nonlinear disturbance such as a bore. Usually, amplitude ordering and dispersive effects result in the leading wavefronts propagating faster than the trailing wavefronts, resulting in a progressive separation of the wavefronts (e.g., Smith et al., 2003, 2005).

After 03:00 UT, the first bore and its associated train of waves began to disappear. By 03:30 UT, only a trace of the leading wavefront was visible followed by a region of chaotic and turbulent airglow. The leading wavefront continued to dissipate and disappeared near the southeastern horizon. The background airglow emission remained enhanced, however (Figure 3), because of the underlying large-scale gravity wave which appeared to generate the bore.

3.2. Satellite Data

Four hours prior to the bore events, at 22:02:46 UT, the NASA TIMED satellite passed over the Asiago site and the on board SABER instrument obtained OH emission and neutral temperature altitude profiles (see Figure 4). Maximum OH emission occurred at 88.5 km with a full width at half maximum (FWHM) thickness of 6.7 km (Figure 4a). The MLT temperature profile exhibited a large 30 K temperature inversion (i.e., increase) between 90 km and 94 km, as well as a weaker inversion extending from 82 km to 90 km (Figure 4b). As a result, the temperature structure yielded a ducting region centered near 96–97 km altitude with a FWHM width of 4.4 km (Figure 4c). Bores require a stable ducting region (such as created by a

Table 1
Measured Parameters Associated With Dual Bore Wave Disturbances Observed Over Asiago on 11 March 2013

	Occurrence time (UT)	$\bar{c}_{obs}$ (ms^{-1})	$\bar{c}_{int}$ (ms^{-1})	λ_x (km)	φ (°E of N)	T_{obs} (min)	T_{int} (min)	$\bar{a}_{obs}$ (ms^{-1} h^{-1})
			Bore #1					
O(^{1}S)	02:06:27	80.1 ± 2.6	131.4 ± 9.4	34.7 ± 3.7	138° ± 1°	7.2 ± 0.8	4.4 ± 0.8	−5.3
OH	02:06:01	76.8 ± 9.5	63.3 ± 15.4	16.5 ± 0.9	138° ± 1°	3.6 ± 0.6	4.3 ± 1.3	−
			Bore #2					
O(^{1}S)	02:34:22	53.7 ± 8.5	106.6 ± 15.2	34.4 ± 6.3	147° ± 1°	10.7 ± 3.7	5.4 ± 1.8	−18.8
OH	02:40:55	47.0 ± 4.1	25.1 ± 9.0	19.1 ± 1.1	147° ± 1°	6.8 ± 1.0	12.7 ± 5.3	−10.7

Note: Occurrence time: image time stamp of first detection; $\bar{c}_{obs}$: observed horizontal wave phase speed; $\bar{c}_{int}$: intrinsic horizontal wave phase speed; λ_x: horizontal wavelength; φ: propagation azimuth; T_{obs}: observed wave period; T_{int}: intrinsic wave period; and $\bar{a}_{obs}$: observed horizontal wave acceleration.
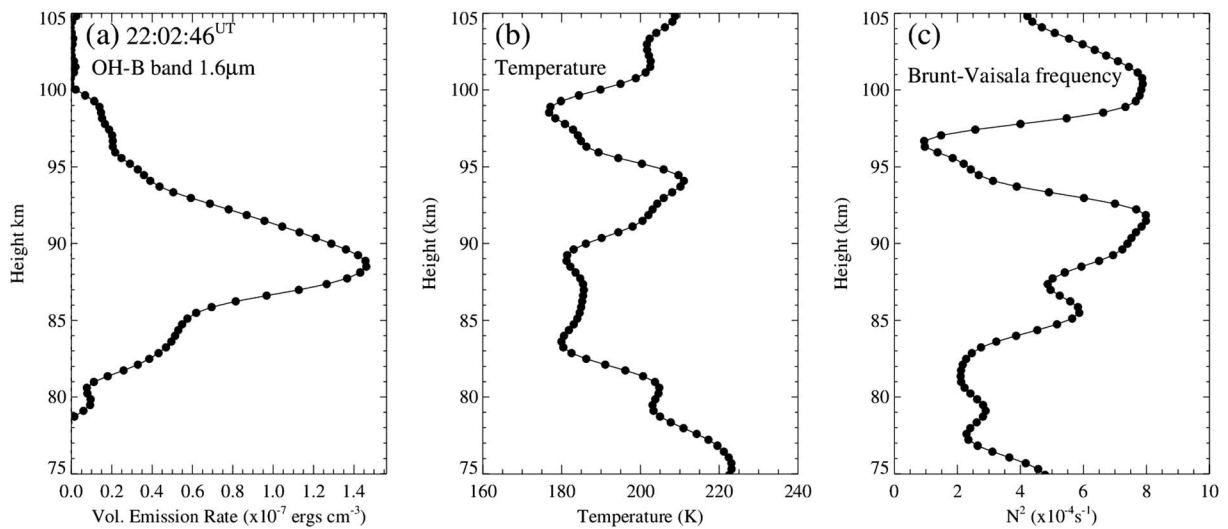
Figure 4. SABER measurements obtained neat Asiago 4 h prior to bore onset. (a) OH emission profile showing maximum emission located near 89 km altitude. (b) The temperature profile exhibits a large 30 K temperature inversion near 90–95 km altitude and a weaker inversion also at 82 to 90 km. (c) The resulting N^2 profile indicates a broad region favorable for trapping and ducting gravity waves.

temperature inversion or wind shear) in which to propagate. Temperature inversions tend to be long-lived phenomena so it is reasonable to assume that the inversion observed by SABER, and hence the duct, was still present 4 h later. In any case, the appearance of the twin bores indicated that a suitable ducting region was present and that it was most probably due to the temperature inversion.

3.3. Ground-Based Radar Observations

Neutral zonal and meridional wind profiles were obtained by the University of Leipzig meteor radar at Collm for the 3 day period of 10–12 March 2013. The radar's location is marked as CL in Figure 1. The winds are derived routinely from the specular reflections from meteor trail echoes originating in the 70–110 km altitude region as they drift along with the local wind. A receiving array of five spaced antennae receives the reflected signals, and the winds are derived using interferometry (Jacobi, 2012; Stober et al., 2012). The Collm radar has become part of the Multistatic Multifrequency Agile Radar for Investigation of the Atmosphere meteor radar network (Stober & Chau, 2015).

A least squares fitting routine was used to determine the variations exhibited by the wind fields during the period of 10–12 March. The wind profiles were dominated by a diurnal tidal variation with an amplitude of 20–30 ms^{-1}, which is typical at middle- to high-latitude sites (e.g., Lu et al., 2011; She, Tao, et al., 2004).

Figure 5 shows component of the neutral horizontal wind at 5 km intervals over the 80 to 100 km altitude region, in the direction of bore propagation, around the time of the double event. Wind values at 1 km interval were available and analyzed for this study but are not shown in Figure 5 for clarity. The individual wind fields in Figure 5 have been shifted vertically in order to display them more clearly. The zero wind line at each altitude is shown as a horizontal dotted line. The all-sky observations occurred during the time between the two vertical dashed lines. The most striking feature in Figure 5 is that the wind variations exhibited a large-scale upward propagating gravity wave that increased in amplitude with increasing altitude. The zenith crossing time of the leading bore in the
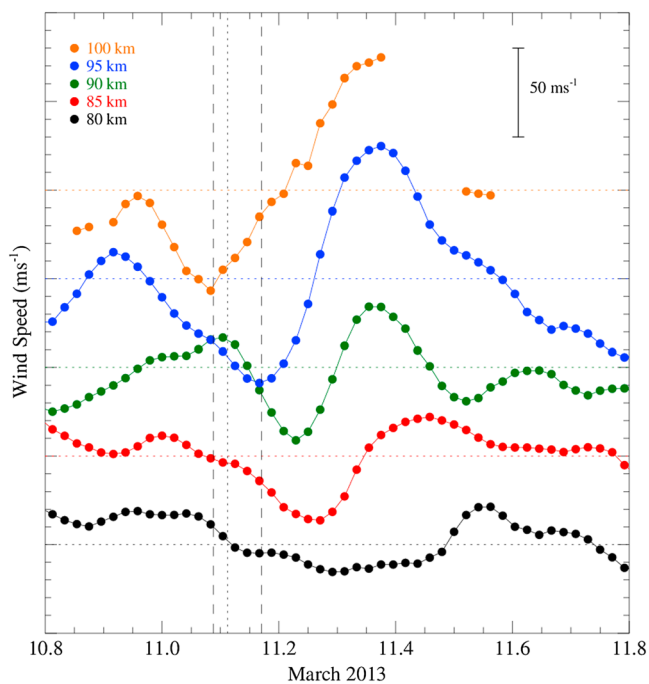

Figure 5. Neutral zonal and meridional wind measurements obtain by the Collm meteor radar at during the 3 day period of 10–12 March 2013 showing the large and unusual tidal wind amplitude that reached 60–70 ms^{-1} during the twin bore event. The vertical line demotes the first bore's zenith crossing time.
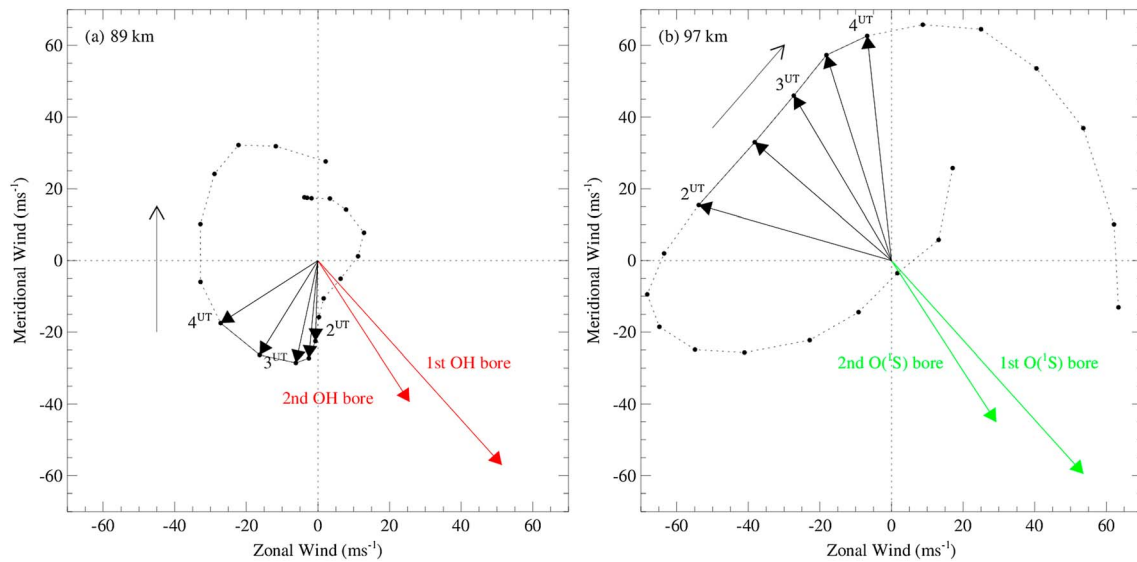
Figure 6. Hodographs of the half-hourly radar wind velocity vectors at Collm at 89 km and 97 km altitude during the night 10–11 March 2013. The clockwise tidal variation is evident as well as the significantly larger wind amplitudes exhibited at 97 km. The five measurements obtained during the 2–4 UT imager observation period are shown as fully drawn vectors. The observed phase velocity vectors of the bores in the OH (red) and O(^{1}S) (green) emissions are also shown.

O(^{1}S) emission (dotted vertical line) occurred when the local wind reached a maximum of 60 ms^{-1} in the opposite direction to the bore propagation (~02:45 UT), which suggests that the disturbance was associated with the large-scale wave. Comparing the relative occurrence times of the wind maxima at 95 km and 100 km in Figure 5 with the zenith crossing time of the O(^{1}S) bore also suggests that the O(^{1}S) emission layer resided near 98 km altitude during that time period.

In particular, on 11 March, around the time of the twin bore event, the wind profiles above 90 km altitude exhibited very large amplitudes of 60–70 ms^{-1}, which is almost 2.5 times larger than typically observed. The first bore passed over the Collm radar site at 02:26 UT (±2 min) with the second bore crossing zenith 15 min later at 02:41 UT (±2 min). The curvature of the first bore partly contributed to the smaller time difference in the zenith crossing times between the first and second bores over Collm compared to that observed at Asiago.

Figure 6 shows the time history of the radar wind vectors, known as hodographs, at the altitudes of the two emission layers—(a) 89 km (OH, red) and (b) 97 km (O(^{1}S), green)—during the observation period. The clockwise variation exhibited by the wind vectors (denoted by the open arrows) is consistent with an upwardly propagating tidal wind field (upward energy propagation and downward phase propagation). The southeastward phase velocity vectors of the bores in each emission are also shown. The observation time period from 2 to 4 UT is also denoted with the measured radar wind vectors. Looking at Figures 6a and 6b, the wind amplitude at 89 km was clearly smaller than at 97 km, and also, the direction of the wind field at the two altitudes was markedly different. At 89 km (Figure 6a), the wind was directed southward and turns westward and exhibited a small component coparallel with the bore propagation direction. At 97 km (Figure 6b), the wind was westward and turned northward and exhibited an almost total antiparallel flow with respect to the bore. From the dispersion equation (see equation (5) further on), if the local wind flow approaches the speed of wave propagation, the term for the intrinsic wave velocity, $c_{int} = c_{obs} - u$ decreases to zero, resulting in the vertical wave number, $m^2(z)$, increasing toward large values (i.e., λ_z tends to zero) and so the wave is absorbed.

The onset of the first bore occurred after the tidal wind vector in the 95–101 km region had rotated toward the northwest, favorable for southeastward wave propagation. The favorable wind field, combined with the ducting region centered near 96–97 km (see Figure 5), above the majority of OH emission (peak at 88.5 km), suggested that the bore propagated at an altitude near the O(^{1}S) emission layer (peak near ~97 km), which would explain why the bore was much brighter in the O(^{1}S) emission yet both exhibited an emission enhancement.
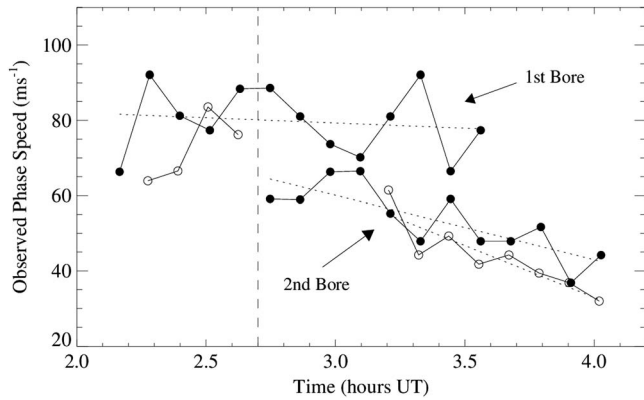
Figure 7. Measured phase speeds of the leading wavefronts associated with the twin bores in O(^{1}S) (solid circles) and OH (open circles) airglow during the course of the night. Both bores exhibited a deceleration over the respective lifetimes (see text). The vertical dashed line indicates the zenith crossing of the first bore.

4. Results and Discussion

4.1. Bore Characteristics

The undular morphology of the bores suggests that we can assume the bore strength parameter (β, see section 1) to be 0.3 or less (undularity). The Brunt-Vaisala frequency (N^2) profile in Figure 4c exhibited a ducting region with a depth (FWHM) of 4.4 ± 0.1 km. That profile was derived from the SABER temperature profile obtained at 22:02:46 UT (Figure 4b) (about 4 h before the first bore appeared in the field of view of the imager). As a result, $h_0 = 2.2 \pm 0.1$ km (FWHM/2.0) and assuming $\beta = 0.3$, yielded a post-bore depth of $h_1 = 2.9 \pm 0.1$ km, and the trailing wave amplitude associated with the bore of $a = 0.5 \pm 0.2$ km (as defined in Dewan & Picard, 1998).

During the 2 h observation period, the phase speed of the first O(^{1}S) bore decreased at a rate of 5.3 ms^{-1} h^{-1}. In comparison, the second O(^{1}S) bore decreased at a rate of 18.8 ms^{-1} h^{-1}, a rate six times larger (see Figure 7) than the first bore. The addition rate of trailing waves associated with the second bore increased during this time period and so we can assume that the decrease in the observed phase speed was the results of energy loss via the addition of the trailing waves. The second bore in OH emission decelerated at a comparable rate to the O(^{1}S) emission. There was insufficient data to quantify accurately the velocity change associated with the first bore in the OH emission. It is assumed to be comparable to what was exhibited in the O(^{1}S) emission. The second bore decelerated at comparable rates in both emissions suggesting similar rates of energy dissipation in that event.

Using equation (4) and the derived bore parameters above, including the background wind, we obtained a theoretical wave formation rate of 2.7 ± 4.9 waves h^{-1}. As shown in Figure 8, image analysis of the first bore in the O(^{1}S) emission yielded a rate that ranged from 4.3 to 8.6 h^{-1}, larger than the theoretical prediction. The largest source of error was due to the estimation of the depth of ducting region (h_0) from the SABER temperature profile. The profile was obtained 4 h prior to the bore events and so may have changed during the intervening hours. The value for the duct depth (h_1) after the passage of the bore assumed the undularity was close to $\beta = 0.3$, the upper limit of undularity (Lighthill, 1978). The amplitude of the bore (a) was also determined by the two duct parameters h_0 and h_1. The wave formation rate is dependent on the change in the cube of the duct depth and also on the square of the bore amplitude. Errors in those parameters could yield a result markedly different to the rate derived via image analysis.

The wave formation rate associated with the Asiago bore is clearly much larger than the model estimate. However, the measured wave formation rate was within the range found in several bore events reported
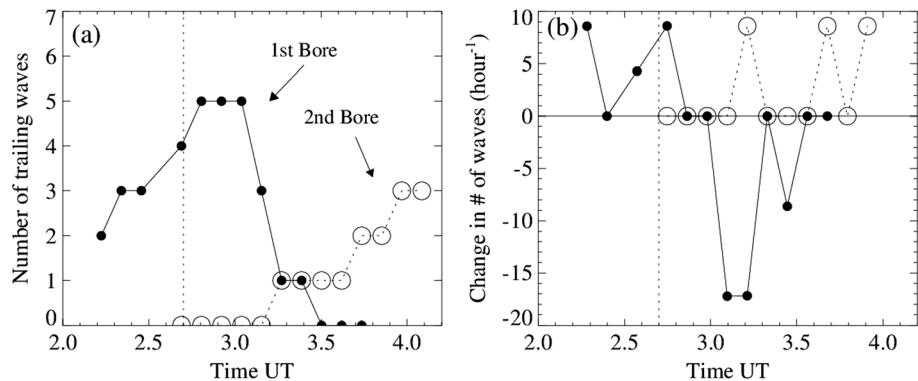

Figure 8. (a) Number of trailing waves associated with the bores in O(^{1}S) emission during the course of the night. Both exhibited similar rates of increase in the number of trailing waves. The first bore exhibited a sudden decrease in the number of waves after 3:00 UT as the entire train began to transform into a trailing region of turbulence. (b) Rate change in the number of waves associated each bore. The rapid rate in the number of waves associated with the first bore is clearly evident.
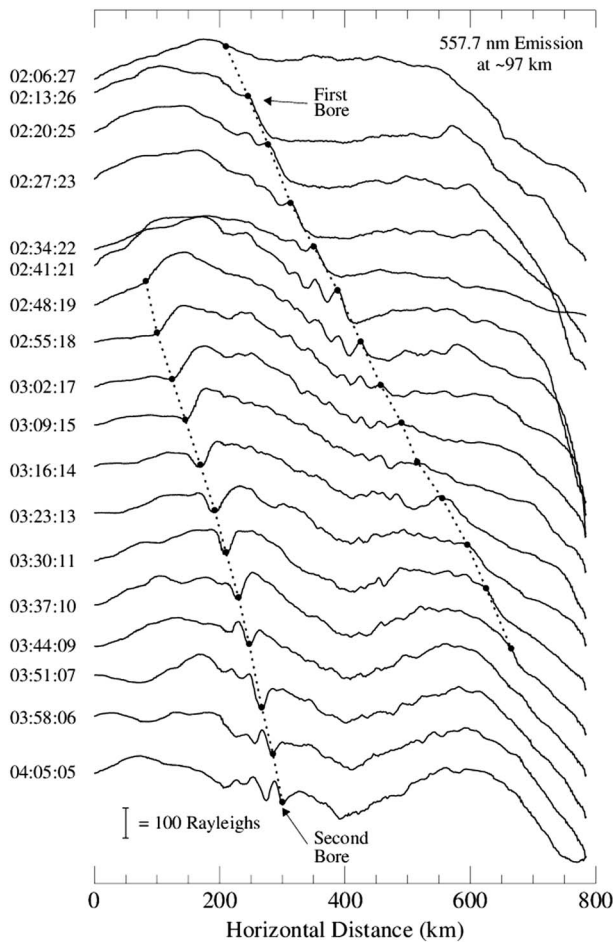
Figure 9. Time series of 557.7 nm image cross sections obtained during the course of the night and which illustrates the dual relationship and time evolution of the two bore disturbances.

previously: 1.3–1.6 h^{-1} (She, Li, et al., 2004), 1.5–2.5 h^{-1} (Smith et al., 2003), 2.8 h^{-1} (Dewan & Picard, 1998; Taylor et al., 1995), 3.3 h^{-1} (Narayanan et al., 2009), 4 h^{-1} (Bageston et al., 2011), and 6.6 h^{-1} (Nielsen et al., 2006). Comparing Figure 2 and Figure 8, the first bore also exhibited a rapid decrease in the number of waves as the entire wave train began breaking into a trailing region of turbulence.

The theoretical estimate assumes a zero background wind. During the lifetime of the first bore, the local wind field above 90 km was directed largely antiparallel to the bore direction and ranged from 60 to 70 ms^{-1} resulting in an intrinsic phase speed of the bore ($c_{obs} - u$) of 120–130 ms^{-1}. Here c_{obs} is the phase speed of the wave and u is the wind speed along the wave direction. From equation (4), the wave formation rate is proportional to the bore speed. As a consequence, the large relative local wind (70–75 ms^{-1} at 96 km altitude and opposite in direction to the 80 ms^{-1} propagation speed of the bore) would have contributed to a larger than expected dissipation rate of the bore. Hence, the 2 h lifetime of the bore was noticeably shorter than for bores of this amplitude. In addition, from equation (3), the bore propagation velocity is determined by the ducting depth. The fact that the two bores each had significantly different phase velocities (~80 ms^{-1} and ~50 ms^{-1}) therefore suggests that the duct depth may have decreased by a factor of 2 after the passage of the first bore. The small time difference (<30 min) between the first and second bores suggests that the reduction in the bore depth occurred rapidly, most probably caused by the turbulent region trailing the first bore that formed after ~02:40 UT.

Figure 9 shows a series of image cross sections obtained from the 557.7 nm images during the course of the night. The cross sections were obtained by sample averaging a 9 pixel wide strip across the image along the direction of wave propagation. Time increases down the figure. The time evolution of both bore disturbances are exhibited clearly and provide the context in which to illustrate their relationship. At first mutual appearance (02:41 UT), the horizontal separation between the leading wavefronts associated with the two bore events was 358 ± 2 km. The separation had increased to 429 ± 2 km (at 03:37 UT) at the end of the night, due to the higher phase velocity of the first bore. The mean horizontal separation of the two bores was 392 km (σ = 23 km).

Figure 9 also illustrates the most important feature of these two events: both bores appear to have formed and evolved atop the leading edges of a larger-scale feature of enhanced airglow emission. This point is particularly evident in the image cross sections in Figure 9 obtained after 03:16 UT when the entire double bore event was sampled in the imager's field of view. The first bore formed on the leading edge of this larger-scale brightening and was exhibited as a bright bore, that is, the background level of emission was enhanced following its passage. The second bore formed on the trailing edge of the feature and was associated with a reduction in the background level of airglow emission, a dark bore. This dual aspect is most clearly exhibited around 02:48 UT, just prior to the formation of the second bore on the trailing edge of the feature. It is also possible that the bores were each formed by successive pulses of wave energy akin to a localized forcing "piston" mechanism suggested by Dewan and Picard (2001). We suggest that both bores formed as instabilities that arose on the leading edges two larger-scale surges separated by 30 min temporally and possibility associated with a wave-like variation of approximately 400 km in extent. Such behavior is consistent with the results of a number of previous modeling studies (e.g., Laughman et al., 2009; Seyler, 2005) that have shown that mesospheric bores may form from a large-scale, large-amplitude gravity wave propagating within a ducting region. The propagating ducted linear wavefronts steepen and develop into nonlinear undular bores according to nonlinear theory. The subsequent observed temporal separation of the wavefronts within each bore is also consistent with previous modeling results.
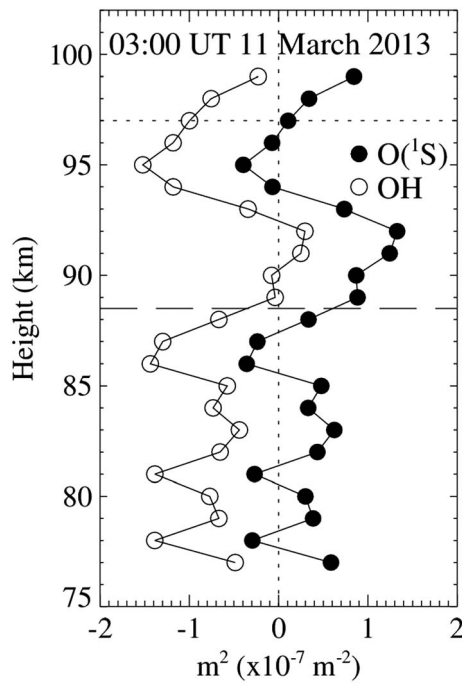
Figure 10. Vertical wave number profiles for 03:00 UT 11 March 2013 calculated from the Taylor-Goldstein dispersion equation using the measured OH and $O(^1S)$ bore parameters, the SABER temperature and OH emission data, and the Collm meteor radar wind data (see text). The altitudes of the OH and $O(^1S)$ emission layers are shown as dotted and dashed lines, respectively.

Using the measured temperature and wind profiles, one can apply the Taylor-Goldstein equation to characterize the gravity wave propagation environment of the region:

$$m^2(z) = \frac{N^2}{(c_{obs} - u)^2} + \frac{u_{zz}}{(c_{obs} - u)} - \frac{u_z}{H(c_{obs} - u)} - k^2 - \frac{1}{4H^2}. \quad (5)$$

Equation (5) indicates that gravity wave propagation is determined by the local temperature and wind fields, via N and u, respectively. Here N is the Brunt-Vaisala frequency, u is the mean wind flow in the direction of wave propagation, c_{obs} is the observed horizontal wave phase speed, u_{zz} is the curvature of the wind flow, u_z is the gradient of the wind flow, H is the scale height, and k ($=2\pi/\lambda_h$) and m ($=2\pi/\lambda_z$) are the horizontal and vertical wave numbers, respectively. Using the measured temperature and wind profiles and wave parameters, equation (5) yields a vertical wave number profile that is unique to the wave. Equation (5) assumes that the vertical-scale sizes of wind and temperature profiles are large compared to vertical wavelength (WKB approximation); however, during the bore event, the vertical wavelength varied considerably. For example, within the 88–94 km altitude region, λ_z ranged from 17 km to 57 km with a mean of 32 km. As a result, equation (5) may not provide an accurate estimation when the vertical wave number is small.

Figure 10 shows the calculated vertical wave number (m^2) as a function of height for the first bore in the OH and $O(^1S)$ emissions at 03:00 UT. Each profile is unique to the bore parameters exhibited in each emission and propagation is permitted only where $m^2 > 0$. For the $O(^1S)$ emission (solid circles), regions of evanescence occurred near 87 km and 95 km. Allowed propagation occurred near 93 km and also above the expected altitude of the emission layer (dotted line) at 97 km. For the OH emission (open circles), a narrow region of allowed propagation occurred only at 90–92 km, slightly above the altitude of the OH emission layer (dashed line). This would explain the weaker emission response in the OH emission.

4.2. Source Identification

The wavefronts associated with the first bore were strongly curved, suggesting that the source region of the bore was relatively localized. The position of the leading wavefront was measured at three locations along the wavefront from five $O(^1S)$ images obtained during the period 02:13–02:48 UT. Using these positions, the radius of curvature and the location of the center were calculated using the formula, $r^2 = (x - x_c)^2 + (y - y_c)^2$, where r is the radius of the curvature, (x_c, y_c) are the center coordinates of the circle. Estimates of the radius of curvature from the five $O(^1S)$ images yielded a remarkably consistent radius of 948 ± 78 km (±8.2%), which located the center of curvature, and region of origin, over southeastern United Kingdom (see Figure 11 and also Figure 1). The red solid bar indicates the standard deviation of the determined mean center of curvature (solid red triangle) in latitude and longitude.

The measured phase speed yielded an estimated travel time of 3 h and 20 min and the time of origin to be 00:22 UT, which provided an upper limit of 3 h for the formation time of the bore. As a comparison, numerical modeling by Seyler (2005) yielded bore formation times of ~2 h and by Laughman et al. (2009), shorter than ~2 h. Dewan and Picard (2001), using a long-term global average of gravity wave-driven momentum deposition, estimated the formation time of a mesospheric bore propagating with a speed of 60 ms^{-1} to be 12 h. An intense episode of gravity wave energy injected into the upper atmosphere such as in the present case could be expected to occur on time scales less than that. The travel time for gravity waves with periods of ~10 min to reach the 95 km altitude region from the upper troposphere is ~50–60 min (e.g., Sentman et al., 2003), so it is feasible that the piston model formation model could provide the forcing in the observed time either to create a mesospheric thermal duct or the bore itself.

Prior to the disturbance, a large and intense frontal storm system moved southeastward over the United Kingdom and western Europe bringing sudden cold temperatures and snow. Tropospheric frontal systems
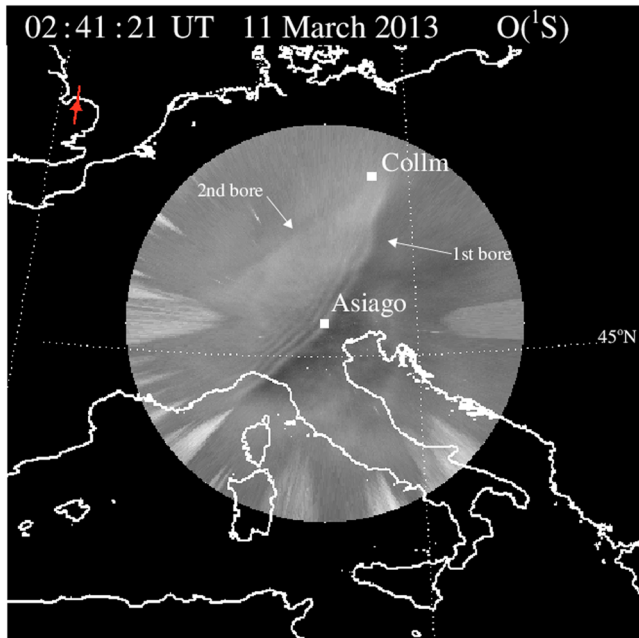
Figure 11. O(^{1}S) image showing the relative positions of the double bores as they propagate southeastward over Asiago. The position of each bore is arrowed. The red triangle located over the southern UK denotes the mean center of curvature of the leading wavefront of the first bore during the period 02:13–02:48 UT suggesting a localized origin for the disturbance.

are synoptic-scale (approximately thousands of kilometers) weather features that are known to be strong sources of gravity waves (e.g., Plougonven & Zhang, 2014). A section of the isobaric analysis chart produced by the UK Meteorological Office for 11 March 2013 at 00:00 UT is shown in Figure 12. The orientation of the frontal system corresponded to the alignment of the wavefronts associated with the bores. Previous bore events have noted the association between large tropospheric frontal weather systems and mesospheric bore events. For example, Smith et al. (2003) reported on the occurrence and alignment of a large naked eye bore over Texas during the presence of a large cold frontal system extending over the United States. More recently, Yue et al. (2010) reported on a similar coincidence using 5 years of bore observations over the Midwest United States.

The association of frontal weather systems with upper atmospheric wave phenomena such as bores suggests that significant amounts of wave energy can be transported routinely to high altitudes from ground level and potentially affect the upper neutral atmosphere and ionosphere.

In order to propagate from the troposphere to MLT altitudes, gravity waves require phase speeds greater than the background local wind field at all levels in order to avoid critical level filtering and absorption. Furthermore, combined observational and ray tracing modeling studies are required in order to better understand the possible relationship and mechanisms between frontal systems and mesospheric bores, a topic that has important implications for the poorly understood and researched terrestrial weather-generated effects on the upper atmosphere.
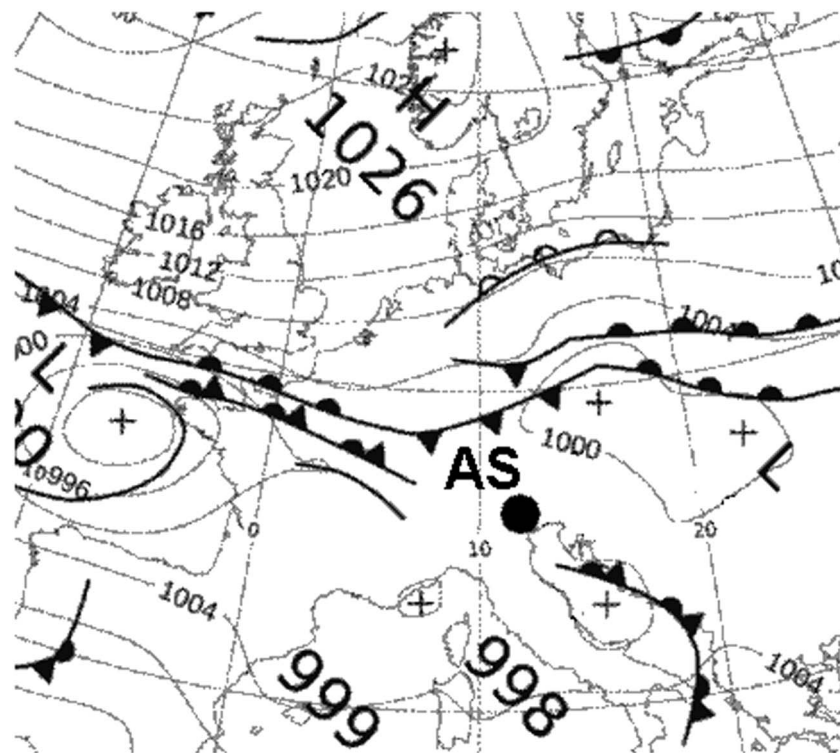

Figure 12. Section of the isobaric analysis chart produced by the UK Meteorological Office for 11 March 2013 at 00:00 UT. The large frontal system described in the text lies to the south of UK (top left) and over western Europe. The location of Asiago is labeled as "AS."

Although the characteristics of mesospheric bores are generally understood, their origin is poorly studied to date. This is related to their relatively low occurrence rate of ~1 per month at midlatitudes (Smith, 2013). The most effective method of investigating their origins and characteristics would be to utilize a cluster of instrumentation tasked with MLT investigations and that is able to adequately characterize a serendipitous bore event when they may occur. An example of such a cluster would consist of` (i) a multispectral all-sky imager to provide the identification, 2-D context, and other gravity wave parameters; (ii) a meteor radar to provide MLT wind profile data over the 70–110 km altitude region; and (iii) a resonance lidar to provide simultaneous MLT temperature profile data. The observational data would be combined with meteorological data from ground level to the upper atmosphere such the ECMWF (European Centre for Medium-Range Weather Forecasts) analysis data to provide the information to link the different regions of the atmosphere.

5. Summary

We have presented observations of a twin mesospheric bore event that occurred over the Padua Observatory in Asiago during the night of 11 March 2013. Analysis suggested that both events were associated with a single, larger-scale mesospheric disturbance and that each bore formed and evolved along the leading and trailing edges of the larger disturbance, respectively. The event also indicated the importance of severe tropospheric weather on influencing or generating remote phenomena within the upper atmosphere and ionosphere, particularly regarding the transport of energy and momentum to those regions, a topic that is poorly understood and researched currently yet is of great importance to the scientific community. A cluster of instrumentation optimized for MLT observations and meteorological data and measurements, as described above, would provide a means to characterize quantitatively, by case history and by statistical means, the formation and evolution of mesospheric bore events. The results would allow also a comparison of bore formation theory: the Dewan and Picard's (2001) piston theory and the instability modeling work done by Laughman et al. (2009) and Seyler (2005).

References

Bageston, J. V., Wrasse, C. M., Batista, P. P., Hibbins, R. E., Fritts, D. C., Gobbi, D., & Andrioli, V. F. (2011). Observation of a mesospheric front in a thermal-Doppler duct over King George Island, Antarctica. *Atmospheric Chemistry and Physics*, *11*, 12,137–12,147. https://doi.org/10.5194/acp-11-12137-2011

Bageston, J. V., Wrasse, C. M., Hibbins, R. E., Batista, P. P., Gobbi, D., Takahashi, H., … Denardini, C. M. (2011). Case study of a mesospheric wall event over Ferraz station, Antarctica (62°S). *Annales de Geophysique*, *29*, 209–219.

Barth, C. A., & Hildebrandt, A. F. (1961). The 5577 A airglow emission mechanism. *Journal of Geophysical Research*, *66*(3), 985–986. https://doi.org/10.1029/JZ066i003p00985

Bates, D. R., & Nicolet, M. (1950). The photochemistry of atmospheric water vapor. *Journal of Geophysical Research*, *55*(3), 301–327. https://doi.org/10.1029/JZ055i003p00301

Batista, P. P., Clemesha, B. R., Simonich, D. M., Taylor, M. J., Takahashi, H., Gobbi, D., … Medeiros, A. F. (2002). Simultaneous lidar observation of a sporadic sodium layer, a "wall" event in the OH and OI 5577 airglow images and the meteor winds. *Journal of Atmospheric and Solar-Terrestrial Physics*, *64*, 1327–1335.

Baumgardner, J., Wroten, J., Mendillo, M., Martinis, C., Barbieri, C., Umbriaco, G., … Hairston, M. (2013). Imaging space weather over Europe. *Space Weather*, *11*, 69–78. https://doi.org/10.1002/swe.20027

Baumgardner, J., Wroten, J., Semeter, J., Kozyra, J., Buonsanto, M., Erickson, P., & Mendillo, M. (2007). A very bright SAR arc: Implications for extreme magnetosphere-ionosphere coupling. *Annales de Geophysique*, *25*, 2593–2608.

Brown, L. B., Gerrard, A. J., Meriwether, J. W., & Makela, J. J. (2004). All-sky imaging observations of mesospheric fronts in OI 557.7 nm and broadband OH emissions: Analysis of frontal structure, atmospheric background conditions, and potential sourcing mechanisms, Bores. *Journal of Geophysical Research*, *109*, D19104. https://doi.org/10.1029/2003JD004223

Dewan, E. M., & Picard, R. H. (1998). Mesospheric bores. *Journal of Geophysical Research*, *103*(3), 6295–6305. https://doi.org/10.1029/97JD02498

Dewan, E. M., & Picard, R. H. (2001). On the origin of mesospheric bores. *Journal of Geophysical Research*, *106*(3), 2921–2927. https://doi.org/10.1029/2000JD900697

Fechine, J., Medeiros, A. F., Buriti, R. A., Takahashi, H., & Gobbi, D. (2005). Mesospheric bore events in the equatorial middle atmosphere. *Journal of Atmospheric and Solar-Terrestrial Physics*, *67*(17–18), 1774–1778.

Fechine, J., Wrasse, C. M., Takahashi, H., Medeiros, A. F., Batista, P. P., Clemesha, B. R., … Russell, J. M. (2009). First observation of an undular mesospheric bore in a Doppler duct. *Annales de Geophysique*, *27*, 1399–1406.

Jacobi, C. (2012). 6 year mean prevailing winds and tides measured by VHF meteor radar over Collm (51.3°N, 13.0°E). *Journal of Atmospheric and Solar-Terrestrial Physics*, *78/79*, 8–18. https://doi.org/10.1016/j.jastp.2011.04.010

Laughman, B., Fritts, D. C., & Werne, J. (2009). Numerical simulation of bore generation and morphology in thermal and Doppler ducts. *Annales de Geophysique*, *27*, 511–523.

Lighthill, M. J. (1978). *Waves in Fluids*(pp. 504). Cambridge, UK: Cambridge University Press.

Lu, X., Liu, A. Z., Oberheide, J., Wu, Q., Li, T., Li, Z., … Franke, S. J. (2011). Seasonal variability of the diurnal tide in the mesosphere and lower thermosphere over Maui, Hawaii (20.7°N, 156.3°W). *Journal of Geophysical Research*, *116*, D17103. https://doi.org/10.1029/2011JD015599

Medeiros, A. F., Paulino, I., Taylor, M. J., Fechine, J., Takahashi, H., Buriti, R. A., … Wrasse, C. M. (2016). Twin mesospheric bores observed over Brazilian equatorial region. *Annales de Geophysique*, *34*, 91–96. https://doi.org/10.5194/angeo-34-91-201

Medeiros, A. F., Takahashi, H., Buriti, R. A., Fechine, J., Wrasse, C. M., & Gobbi, D. (2005). Response of OH, O_2, and OI5577 airglow emissions to the mesospheric bore in the equatorial region of Brazil. *Advances in Space Research*, *35*, 1,971–1,975.

Mendillo, M., Barbieri, C., Baumgardner, J., Wroten, J., Cremonese, G., & Umbriaco, G. (2012). A stable red auroral arc over Europe. *Astronomy and Geophysics*, *53*, 16–18.

Mendillo, M., Baumgardner, J., Wroten, J., Martinis, C., Smith, S., Merenda, K. -D., … Barbieri, C. (2013). Imaging magnetospheric boundaries at ionospheric heights. *Journal of Geophysical Research: Space Physics*, *118*, 7294–7305. https://doi.org/10.1002/2013JA019267

Narayanan, V. L., Gurubaran, S., & Emperumal, K. (2009). A case study of a mesospheric bore event observed with an all-sky airglow imager at Tirunelveli (8.7°N). *Journal of Geophysical Research*, *114*, D08114. https://doi.org/10.1029/2008JD010602

Nielsen, K., Taylor, M. J., Stockwell, R. G., & Jarvis, M. J. (2006). An unusual mesospheric bore event observed at high latitudes over Antarctica. *Geophysical Research Letters*, *33*, L07803. https://doi.org/10.1029/2005GL025649

Plougonven, R., & Zhang, F. (2014). Internal gravity waves from atmospheric jets and fronts. *Reviews of Geophysics*, *52*, 33–76. https://doi.org/10.1002/2012RG000419

Sentman, D. D., Wescott, E. M., Picard, R. H., Winick, J. R., Stenbaek-Nielsen, H. C., Dewan, E. M., … Morrill, J. (2003). Simultaneous observations of mesospheric gravity waves and sprites generated by a midwestern thunderstorm. *Journal of Atmospheric and Solar-Terrestrial Physics*, *65*, 537–550.

Seyler, C. E. (2005). Internal waves and undular bores in mesospheric inversion layers. *Journal of Geophysical Research*, *110*, D09S05. https://doi.org/10.1029/2004JD004685

She, C. Y., Li, T., Williams, B. P., Yuan, T., & Picard, R. H. (2004). Concurrent OH imager and sodium temperature/wind lidar observations of a mesopause undular bore event over Fort Collins/Platteville, CO. *Journal of Geophysical Research*, *109*, D22107. https://doi.org/10.1029/2004JD004742

She, C. Y., Tao, L., Collins, R. L., Yuan, T., Williams, B. P., Kawahara, T. D., … Hagan, M. E. (2004). Tidal perturbations and variability in the mesopause region over Fort Collins, CO (41°N, 105°W): Continuous multi-day temperature and wind lidar observations. *Geophysical Research Letters*, *31*, L24111. https://doi.org/10.1029/2004GL021165

Shiokawa, K., Suzuki, S., Otsuka, Y., Ogawa, T., Nakamura, T., Mlynczak, M., & Russell, J. M. (2006). A multi-instrument measurement of a mesospheric front-like structure at the equator. *Journal of the Meteorological Society of Japan*, *84A*, 305–316.

Smith, S. M. (2013). The identification of mesospheric frontal gravity-wave events at a mid-latitude site. *Journal Advances in Space Research, Special Issue: Advances in MLTIS Studies*. https://doi.org/10.1016/j.asr.2013.08.014

Smith, S. M., Friedman, J., Rashida, S., Tepley, C., Baumgardner, J., & Mendillo, M. (2005). Evidence of mesospheric bore formation from a breaking gravity wave event: Simultaneous imaging and lidar measurements. *Journal of Atmospheric and Solar-Terrestrial Physics*. https://doi.org/10.1016/j.jastp.2004.11.008

Smith, S. M., Taylor, M. J., Swenson, G. R., She, C. Y., Hocking, W., Baumgardner, J., & Mendillo, M. (2003). A multi-diagnostic investigation of the mesospheric bore phenomenon. *Journal of Geophysical Research*, *108*(A2), 1083. https://doi.org/10.1029/2002JA009500

Stober, G., & Chau, J. L. (2015). A multistatic and multifrequency novel approach for specular meteor radars to improve wind measurements in the MLT region. *Radio Science*, *50*, 431–442. https://doi.org/10.1002/2014RS005591

Stober, G., Jacobi, C., Matthias, V., Hoffmann, P., & Gerding, M. (2012). Neutral air density variations during strong planetary wave activity in the mesopause region derived from meteor radar observations. *Journal of Atmospheric and Solar-Terrestrial Physics*, *74*, 55–63. https://doi.org/10.1016/j.jastp.2011.10.007

Taylor, M. J., Turnbull, D. N., & Lowe, R. P. (1995). Spectrometric and imaging measurements of a spectacular gravity wave event observed during the ALOHA-93 Campaign. *Geophysical Research Letters*, *22*, 2849–2852. https://doi.org/10.1029/95GL02948

Walterscheid, R. L., Hecht, J. H., Gelinas, L. J., Hickey, M. P., & Reid, I. M. (2012). An intense traveling airglow front in the upper mesosphere–lower thermosphere with characteristics of a bore observed over Alice Springs, Australia, during a strong 2 day wave episode. *Journal of Geophysical Research*, *117*, D22105. https://doi.org/10.1029/2012JD017847

Yue, J., She, C. -Y., Nakamura, T., Harrell, S., & Yuan, T. (2010). Mesospheric bore formation from large-scale gravity wave perturbations observed by collocated all-sky OH imager and sodium lidar. *Journal of Atmospheric and Solar-Terrestrial Physics*, *72*, 7–18.

Erratum

In the originally published version of this article, equation (3) has the term $h_1(h_1 + h_0)/2h_0$ as an exponent of g', when it should have been multiplied by g'. The equation has since been corrected, and this version may be considered the authoritative version of record.